POLITECNICO DI TORINO
UNIVERSITÉ PARIS-DIDEROT

Master's double degree in Nanotechnologies and Quantum devices

Academic year 2018-2019

Towards strong coupling between a single fluorescent molecule and a plasmonic resonator

---

Supervisors

Sébastien Bidault

Carlo Ricciardi

Candidate

Francesca Legittimo

The unique ability of plasmonic nanostructures to confine light into deep subwavelength volumes gives the opportunity to significantly alter the local density of photonic states (LDOS), boosting light-matter interactions at the nanometric scale.
This opens interesting perspectives for fundamental Physics and Nano-optics and for a large range of exciting applications, in particular within the field of Quantum information.
The development of widespread quantum technologies strongly depends on the possibility to exploit the highly non linear response of single quantum emitters to obtain reliable single-photon sources and nanometric optical transistors on chip. However, so far this has been prevented at room temperature by the inherently weak interaction between the electromagnetic radiation and single emitters, due to their very weak absorption cross section.
In the following I will address how it is possible to reach strong coupling between a dye molecule and the elctromagnetic field of a plasmonic nanocavity, discussing the technical issues observed in the current state-of-the-art as well as the work done during my internship to try and overcome them.

CONTENTS

1 INTRODUCTION

1.1 THEORETICAL BACKGROUND

Strong coupling between a dye molecule and the electromagnetic mode of an optical cavity arises when the photons stored in the latter one are coherently and repeatedly exchanged with electronic excitations in the emitter. Qualitatively, this is equivalent to say that the coupling rate Ω has to be higher than both the cavity loss rate and the emitter decay rates,in order to let energy quanta be exchanged many times before escaping the coupled system. [1], [2].
To understand how this regime can be reached, it is necessary to give an overview of the physics of the system and to explain the main parameters involved in the phenomenon.

A molecule is said to be *fluorescent* if, once excited through the absorption of a photon, it can relax to its ground state by emitting a new quantum of light, with a certain emission rate Γ^{RAD} such that the radiative lifetime is in the *ns* range. In addition, the excited electronic level can depopulate through non radiative decay processes, commonly phonon-mediated. It follows that the lifetime of an electron in the upper level is affected by both radiative and non-radiative processes and the total decay rate is given by $\Gamma = \Gamma^{RAD} + \Gamma^{NR}$; the ratio between Γ_{RAD} and Γ is called *Quantum Yield* and, for commercial dye molecules, it is around 60%.
A remarkable property of fluorescence is that the new emitted photons are typically less energetic than the absorbed one; this phenomena can be explained by means of the Jablonski diagram, illustrating the electronic states of a molecule and the transitions between them. As it is possible to appreciate in figure 1.1, each molecular electronic level is made up by several vibrational modes: when an electron is brought into a higher excited state, it will undergo non-radiative dephasing processes, called vibrational relaxation, toward the lowest excited level. The lifetime of the higher states is on the order of *fs*, making the rate of these dephasing mechanisms (γ) much faster than the depopulation decay rate Γ.

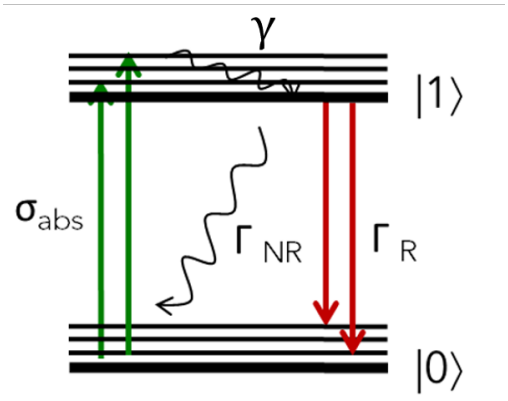

Figure 1.1: Jablonski diagram: Ground state and first excited states with their vibrational levels.

For simplicity, according to the main theory [3], dye molecules in free space are described as two-level dipole emitters, with transition energy $\hbar\omega_0$, total decay and dephasing rate Γ_0 and γ_0

1 It can be described as the polarizability of a classical resonant scatter $\overline{\alpha_0} = \frac{3\pi c^3}{\omega_o^3} \frac{\Gamma^0_{RAD}}{\omega_0 - \omega - i\gamma^0} \mathbf{u} \otimes \mathbf{u}$

respectively, and free-space polarizability $\overline{\alpha_0}$[1].
In a homogeneous background, the induced dipole moment is simply given by

$$\mathbf{d}(\omega) = \overline{\alpha_0}(\omega)\epsilon\mathbf{E_{inc}} \tag{1}$$

The electrodynamic response of a molecules is more complex when it is placed in a structured environment. As it is possible to see in figure 1.2, the dipole is primarily excited by the field $\mathbf{E_{exc}}$ scattered by the environment; the field induced by the dipole also couples to this complex environment, leading to a modification of the power dissipated by this dipole.

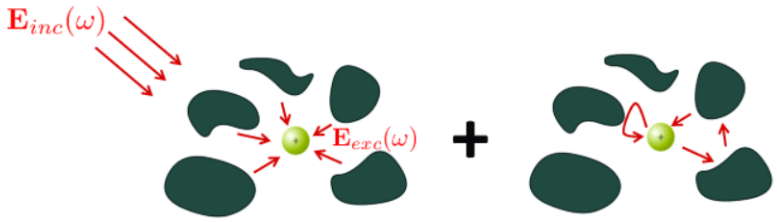

Figure 1.2: Representation of the two scattering processes involved in the electrodynamic interaction between a dipole emitter and a structured environment. Picture re-printed from reference 3

.

As a matter of fact, the environment modifies the local density of optical states around the emitter, increasing the number of decay channels available for the depopulation of the excited state, i.e. for spontaneous emission. However, part of them will correspond to absorption and thus dissipation in the materials surrounding the molecule, resulting in new **external** non-radiative decay processes, while the additional radiative channels, basically due to scattering, will impact on far field emission. This change in radiative and non-radiative density of optical states can be evaluated by means of classical electrodynamics, if normalized to its value in the homogeneous environment [5]; specifically it means that

$$\frac{\rho_p^{RAD}}{\rho_0} = \frac{P^{RAD}}{P_0}; \frac{\rho_p^{TOT}}{\rho_0} = \frac{P^{TOT}}{P_0}; \tag{2}$$

where

- $\rho_0 = \frac{\omega^2}{3\pi^2 c^3}$ is the LDOS in vacuum;
- $\frac{\rho_p^{TOT}}{\rho_0}$, called *Purcell factor* (F_m), will be an extremely important parameter for the following work;
- P_0 is the power radiated by a dipole in a free-background;
- P^{RAD}, P^{TOT} are respectively the radiated and total dissipated power by the dipole in the structured environment.

It is worthwhile to notice that the normalization factor are equal for the total and the radiative part of equations 2. This occurs since the environment does not affect the **internal** non-radiative depopulation processes, but only the paths available for the emitted photons.

For all these reasons, equation 1 is not valid any more: it is necessary to define a new *Dressed* polarizability, dependent on both the emitter and the environment responses, such that $\mathbf{d}(\omega) = \overline{\alpha}(\omega)\epsilon\mathbf{E_{exc}}$.

The poles in $\overline{\alpha}(\omega)$ define the eigenmodes of the coupled emitter-field system, with central frequency ω_p and linewidth γ_p (complex eigenfrequency $\overline{\omega_p} = \omega_p - i\gamma_p/2$).

Let's now analyze the peculiar case of an emitter resonant or quasi-resonant with a specific mode (central frequency ω_m and linewidth γ_m) of an optical cavity.
Following the procedure reported in ref. [1], it is possible to find two solutions $\overline{\omega_p^+}, \overline{\omega_p^-}$ for the complex frequency of the coupled-system:

$$\overline{\omega_p^{\pm}} = \frac{\overline{\omega_0} + \overline{\omega_m}}{2} \pm \sqrt{\left(\frac{\overline{\omega_m} - \overline{\omega_0}}{2}\right)^2 + \Omega^2} \tag{3}$$

where

- $\overline{\omega_0} = \omega_0 + i(\gamma_0 - \Gamma_0)/2 \sim \omega_0 + i\gamma_0/2$;
- $\overline{\omega_m} = \omega_m + i\gamma_m/2$;
- Ω coupling strength.

When $\Omega^2 \gg \left(\frac{\overline{\omega_0}+\overline{\omega_m}}{2}\right)^2$ equation 3 suggests a split of $\overline{\omega_p^{\pm}}$ with respect to the average resonance frequency of the initially uncoupled systems, with distance proportional to Ω. This process, known as Rabi Splitting, is a signature of strong coupling regime and can be experimentally observed if the frequency separation is bigger than the linewidth of the new eigenmodes.
Contrarily, if $\Omega^2 < \left(\frac{\overline{\omega_0}+\overline{\omega_m}}{2}\right)^2$ the two systems would be only slightly modified and, according to Fermi Golden rule, the change in the molecule total decay rate could be written as $\frac{\Gamma_p}{\Gamma_0} = F_m$.
Even if the previous equivalence is valid only in the weak coupling regime, the Purcell factor is a fundamental parameter also for higher coupling strengths, being

$$\Omega = \sqrt{\frac{F_m \Gamma_0^{RAD} \gamma_m}{4}} \tag{4}$$

It follows that, for $\omega_0 \sim \omega_m$ the system enters in strong coupling regime for

$$\frac{4\Gamma_0^{RAD}\gamma_m F_m}{(\gamma_m - \gamma_0)^2} > 1 \tag{5}$$

Equation 5 clearly shows that a good spectral match between the emitter and the cavity mode (i.e. $\gamma_m \sim \gamma_0$ is fundamental to fulfill this requirement; however, it is necessary to analyze the behavior of the numerator too and, among all the parameters playing a role, the Purcell factor deserves a proper discussion.
According to [5], it can be re-written as

$$F_m = \frac{6\pi c^3}{\omega_m^2 \gamma_m} \frac{1}{V_m} = \frac{\lambda_m^3}{4\pi^2} \frac{\omega_m}{\gamma_m} \frac{1}{V_m} = \frac{\lambda_m^3}{4\pi^2} \frac{Q}{V_m} \tag{6}$$

where Q is the Quality factor of the chosen cavity, quantifying the temporal confinement of light in the resonator, and V_m the electromagnetic mode volume, corresponding to the spatial confinement. This latter parameter has a straightforward interpretation only in the case of closed and no-losses cavity. In these conditions it is proportional to $\int \epsilon(\mathbf{r})|\mathbf{E_m}(\mathbf{r})|^2 d\mathbf{r}$, where $\epsilon(\mathbf{r})$ and $\mathbf{E_m}(\mathbf{r})$ is the cavity mode normalized such that its norm is unity at the antinode of the electric field.
However, in a resonator with high leakage of radiation the field eigenmodes expand to infinity in space, making the normalization of the field and of V_m difficult to perform. There is an active and open discussion about this theme among the scientific community[6] , even if the problem is

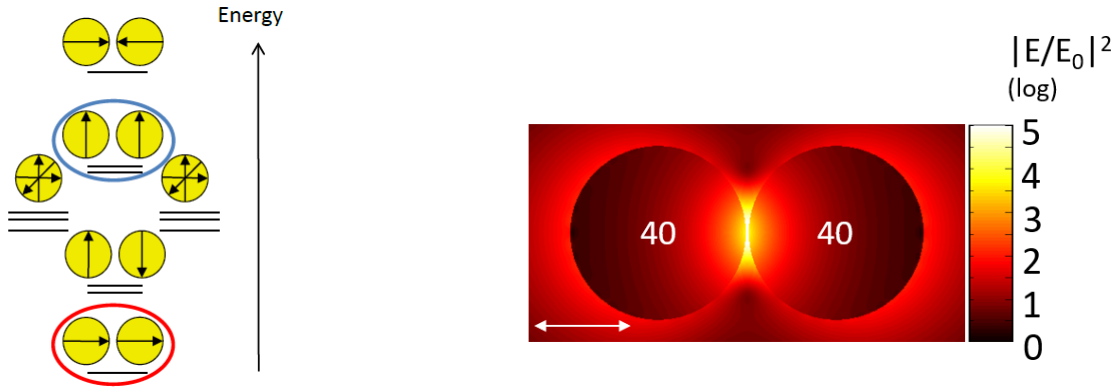

(a) (b)

Figure 1.3: (a)Hybridization of plasmonic modes and (b) field enhancement between two 40nm Au NSs, evaluated by means of Mie theory.

usually overcome simply by introducing perfectly matched layers to force the electric field to reach 0 at a finite distance from the resonator.
The first demonstrations of strong coupling between a single emitter and the electromagnetic mode of a resonator were obtained with the use of dielectric cavities[8], whose mode volume is inevitably bounded by the diffraction limit($\sim (\frac{\lambda_m}{2n})^2$); thus, to fulfill eq. 5, they require high Quality factor,i.e. narrow linewidth, such that their limited coupling strength can overcome the cavity losses. Since, as stated before, for good coupling the emitter spectra should overlap with that of the cavity, this kind of systems require cryogenic cooling to reduce the molecular vibrational dephasing, which makes the molecule bandwidth too large at room temperature. [9] Plasmonic nanostructures offer a route to overcome these issues.

Under appropriate conditions, an incoming electromagnetic field can interact with free electrons in the surface of a metal to yield a hybrid electron/field oscillation mode, called Surface Plasmon Polariton (SPP), strictly bounded to the surface. SPP can be further spatially confined, if they are associated with metallic nanostructures: in this case they are called Localized SPP (LSPP) and show peculiar features, making them interesting for the emitter-field strong coupling regime. The resonance frequency of these oscillating modes usually occurs in the visible range, but strongly depends on the composition, size and shape of the chosen nanoparticle and on its surrounding material ; for the sake of clarity, the properties of the simplest possible system will be analyzed, followed by a straightforward generalization to more complex structures.
When a metallic nanosphere (NS) ($\epsilon_m = \epsilon_1(\omega) + i\epsilon_2(\omega)$) is smaller than the incoming field wavelength ($r \ll \lambda/100$), the phase of the latter one can be considered constant in each point of the nanoparticle, making the Quasi-static approximation valid. In this case, the NS polarizability diverges for $\epsilon_1(\omega) = -2\epsilon_d$, with ϵ_d permettivity of the dielectric medium embedding it, causing the SPP to be excited; being confined in volume, charge oscillations make opposite sides of the sphere to take on opposite charges and the nanoparticle will behave as a dipole, with damping rate given by the imaginary part of ϵ_m. Since the emitted field is distributed around the NP, it is possible to overcome the diffraction limit, obtaining light-confinment in subwavelength volumes that can be made even smaller arranging two nanoparticles in a dimer configuration. Approaching two nanospheres in the quasi-static approximation, in fact, their induced dipole will couple, to form new hybridized modes, as schematize in figure 1.3a.

Only the three highlighted modes still continue to be dipolar, since the dipoles induced in each sphere are in phase. The lowest energy is provided by the longitudinal mode for which the two

dipoles interect cooperatively (highlighted on red): when the particles get closer, the coupling increases and the system requires a lower energy to be resonantly excited, leading to a spectral redshift. The transverse mode, highlighted in blue, corresponds to dipoles that are coupled in a non-cooperative way, leading to a spectral blueshift of the resonance. Overall, the cooperative aspect of the longitudinal mode means that it provides a larger interaction cross-section with the electric field of light and will dominate the optical response of the dimer.
All these considerations were carried out in the restricting quasi-static and dipolar hypotheses. The first one is no longer valid when the NP radius becomes comparable to $\lambda/100$, due to the violation of energy conservation, since all scattering phenomena are neglected. Furthermore, increasing the size of the particle to $\lambda/10$ means that the phase of the electric field cannot be supposed homogeneous over the particle size, leading to the excitation of quadrupolar and higher order modes in a single sphere. In the case of dimers, the full multipolar response is even more complex. However, it is possible to predict the behavior of a nanosphere through the generalized Mie Theory, solution of the Helmholtz equation in spherical coordinates, or through full-wave electrodynamic simulations (such as the MNPBEM matlab toolbox), as it will be discussed in more details in the following pages.

Figure 1.3b, shows the enhancement of the electric field in the vicinity of a 40nm-gold NSs dimer excited by a plane-wave with $\lambda = 658nm$ (resonant frequency of the bright longitudinal mode) and polarization parallel to the dimer axis: the longitudinal mode provides strong field confinement in the interparicle gap (small V_m), large scattering efficiency and intense local field enhancement. This last property is important as, by reciprocity ([7]) , it corresponds to a strong increase of the density of radiative optical states when coupling a fluorescent emitter to such resonator. The other modes, being all quadrupolar, are called Dark modes and are associated with an increase in non-radiative LDOS. It follows that the Purcell factor is expected to be very large in this kind of structures; furthermore, they are open cavity, composed by fairly dissipative elements making their Q-factor in the order of 5-10. As a consequence, their quite broad bandwidth is finally comparable with those of commercial dye molecules in ambient conditions ($\sim 120meV$). For all these properties plasmonic nanocavities are perfect candidates to provide strong-coupling with a quantum emitter at room temperature.

1.2 STATE-OF-ART

1.2.1 *Recent experimental realizations of strong coupling*

In recent years, plasmonic nanocavities coupled with quantum emitters have been intensively studied in plenty of configurations [25], from both theoretical and experimental points of view. Here few particularly meaningful works will be reported, underlining the intrinsic limit of current state-of-art; finally, the work done by S. Bidault and his coworkers to overcome these issues will be briefly addressed.

As early as 2004, Mugnier and colleagues used silver surface plasmon and molecular J-aggregates to observe consistent Rabi splitting [10] and Shegai and his team, in 2012, were able to reach strong coupling between a single silver nanoprism and J-aggregates[26]. However, both these experiments involved hundreds of molecules, obviously increasing the coupling strength.

In 2016, a study carried out by the Department of Chemical Physics at the Weizmann Institute of Science (Israel) demonstrated Rabi splitting at the single quantum emitter limit, using semiconductor quantum dots in the gap of silver bowtie plasmonic cavities [11].
The metallic structure was obtained by means of electron beam lithography while commercial

CdSe/ZnS QDs were positioned in the gap ($\sim 20nm$) exploiting interfacial capillary forces, as shown in figure 1.4a. Even if they were able to obtain Rabi splitting of the order of 200meV for two QDs in the cavity and some samples with 120meV of split in the single QD case, this technique only provides a limited control over the number and especially on the position of emitters in the gap (typical uncertainty of the order of 20 nm).

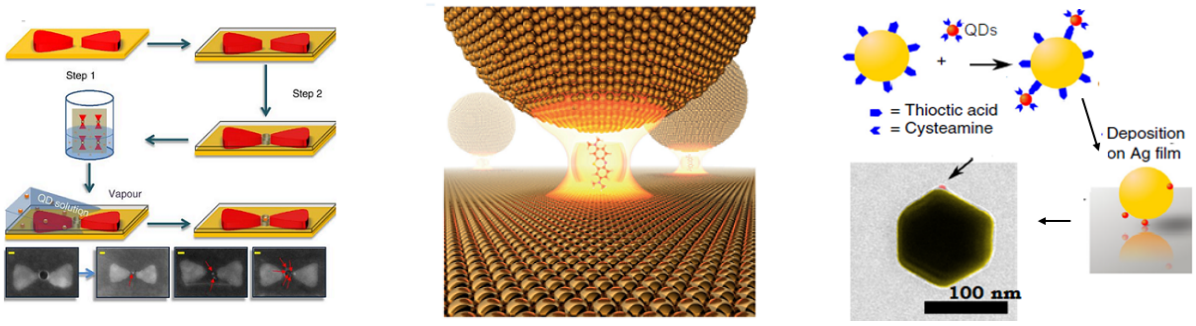

(a) (b) (c)

Figure 1.4: (a) QDs placing mechanism in the bowties silver nanocavities; (b) Nanoparticles-on-mirror geometry with emitter positioned by means of host-guest chemistry; (c) Chemical assembly of colloidal Au NPs and QDs.

A valid alternative to the top-down approach typical of lithography is provided by chemical assembly: in 2016, Baumberg and his colleagues exploited the nanoparticle-on-mirror geometry [12] placing common dye molecules, methylene blue, in the gap between 40nm-gold nanospheres and 70nm-thick gold layer through a host-guest chemistry of macrocyclic cucurbit[n]uril molecules, as shown in figure 1.4b . The latter were designed to contain a single dye, i.e decreasing the ratio between dye and cucurbit[n]uril molecules it is possible, in principle, to work at the single-emitter case. However, the exact number of emitters in the cavity could be only extrapolated from the coupling strength after the measurement. Nevertheless, they demonstrated how fundamental it is to align the transition dipole with the longitudinal dipolar mode of the cavity: by means of Dark field scattering spectra they saw resonant plasmonic peaks identical to those of an empty cavity for emitters parallel to the mirror,while mode splitting occurred only for methylene-blue molecules perpendicular to it.
Two years later, Matthew Pelton and his team showed for the first time consistent Rabi splitting in scattering and fluorescence measurements from individual coupled plasmon–emitter systems consisting of a single colloidal quantum dot in the gap between a gold nanoparticle and a silver film [13]. Also in this case the samples were chemically assembled: Au quasi-spherical NPs and CdSe/CdS QDs were linked covalently through their capping molecules,resulting in a small number of QDs on the surface of each AuNP. Then, depositing the functionalized particles on an Ag film by drop-casting, they obtained nanoparticle-on-mirror cavities with a single dot in the gap. Unfortunately, they reached robust Rabi splitting(g∼200meV) only in 1% of the samples, likely corresponding to QD located at the apex of a faceted AuNP: an example can be seen in figure 1.4c. Metallic structure with corners, tip or generally high curved surfaces go through a strong enhancement of the electric field through a phenomena called *Lightning rod effect*. It is a direct consequence of the continuity condition of the perpendicular dielectric displacement at the boundary, where the charges are sharply accumulated [14]. It follows that the QDs by chance positioned at the edge of a NP facets experience a much higher radiative LDOS, enhancing the coupling strength.
In view of these developments, it is reasonable to conclude that the required nanofabrication achievement for this research field is to obtain a deterministic control on the number of emitters

in the cavity and, equally important, of their position near nanoscale tips.
DNA-mediated chemical assembly can provide the solution to these two requirements, as it has been proven in several works by S. Bidault and his team.

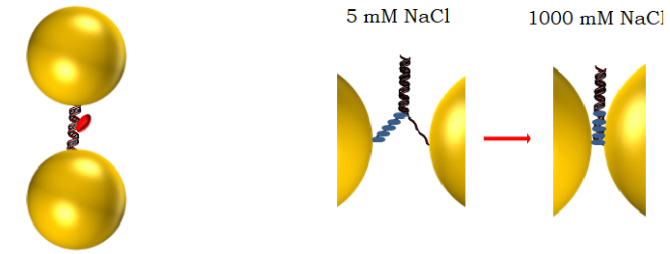

(a) (b)

Figure 1.5: (a)and (b) DNA-mediated dimer assembly in two different configurations

1.2.2 *Emitter-resonator coupling with DNA Nanotechnology*

A single DNA strand is a polymer made up by four different nucleotide bases which selectively hybridize to form a helical double-stranded structure. Thus, a dimer can be formed functionalising two nanoparticles with complementary DNA strands, one of them containing the chosen number of emitters covalently attached in the desired position of the chain. In 2012, S. Bidault & coworkers positioned a single ATTO647N dye molecule precisely in the middle between two 36nm-Au NSs[14]: they employed two 30 bases or 50 bases (bp) DNA complementary sequences, corresponding respectively to 13 ± 1 nm and 17.5 ± 1.5 nm of interparticles distance (see fig. 1.5a). The interaction between emitter and longitudinal plasmonic mode fell in the realm of weak-coupling regime, with a maximum Purcell factor around 100 in the 30bp case. Because of the quantitative agreement between measured rate enhancements and theoretical calculations, they demonstrated a nanometric control over the emitter particle position, with a method allowing to synthesize millions of coupled systems in parallel.
Finding a reliable and reproducible way to obtain robust strong coupling in this configuration is the final aim of J. Heintz's PhD project, tutored by S. Bidault. To further enhance the Purcell factor, they act on the interparticle distance binding DNA-strands and 40nm Au-NPs through a "zipper" strategy, shown in fig.1.5b. Changing the concentration of NaCl in the colloidal solution, it is possible to reduce the electrostatic repulsion between the nanoparticles and to lower the dimer gap up to few nms, leading to a gradual enhancement of the emitters-plasmon coupling. It is pushed up also by the presence of 5 ATTO647N molecules in the gap; the transition dipole orientation of DNA-bound dye molecules is unknown [2] and having 5 molecules instead of one increases the probability of a longitudinal coupling for at least one emitter, together with the interaction strength.
Below some preliminary and motivating results are reported: scattering measurements revealed that 80% of dimers with interparticles distance around 2nm exhibit Rabi splitting higher than 100meV. It is interesting to notice that condition 5, according to BEM simulations discussed later, is expected already for d∼4nm, but the visibility criteria (splitting bigger than the final modes linewidths) requires the above mentioned dimer gap; as a consequence few spectra feature a linewidth broadening without mode splitting that should still correspond to strong coupling(see inset (b)).

2 it has been shown to fluctuate around a preferential axis in the ps range [16]

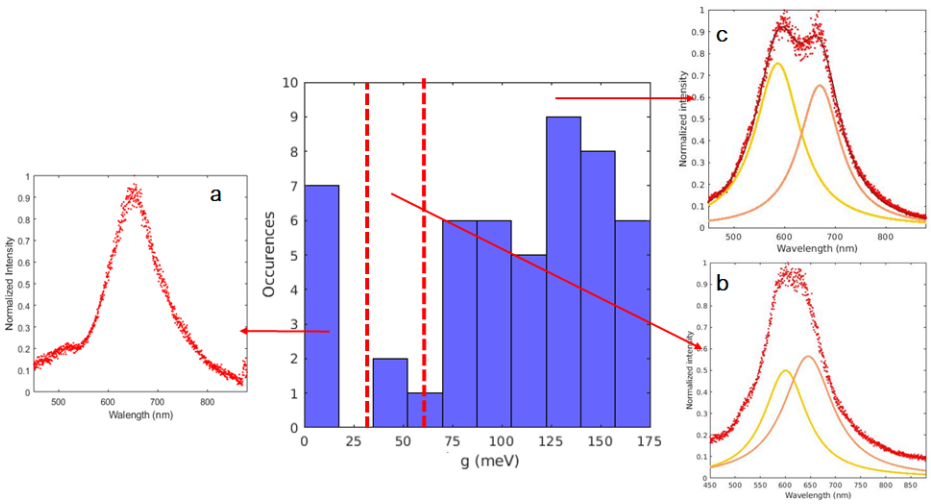

Figure 1.6: Preliminary evidences of strong coupling between 5 ATTO647N molecules and 40nm Au NSs dimers. (a) Spectrum of an uncoupled system; (b) Strong coupling without visible mode splitting (c) Robust Rabi splitting

Unfortunately, an emitter placed so close to a metallic surface experiences high enhancement of the non-radiative decay paths, due to omhic losses of gold electron cloud, finally causing a robust quenching of its fluorescence. In order to recover strong coupling but with large emission quantum yields, the *Ligthning rod effect*, increasing the electric field in the dimer gap and thus by reciprocity the radiative DOS, should provide a solution to this problem. Substituting Au-NSs with nanorods could appear as the most logical choice; however, the resonance wavelength of these systems would fall in the Infrared region, while our range of interest is the visible one. For this reason, the behavior of an emitter placed in between two vertexes of gold 40nm nanocubes was simulated, finding that strong coupling criteria would be verified for higher distances and with large emission efficiency~ 0.5.
Exploring the potentialities of this promising new system is the purpose of my internship.

1.2.3 *Internship project*

In the following chapters I will address the work done during the last months. First of all, I will characterize extinction and scattering spectra of single gold and silver nanocubes in order to verify that electrodynamic simulations are well-suited to estimate their optical response. The choice to investigate also Ag properties is dictated from its lower absorption and damping rate with respect to gold [17],[18] which could be meaningful to reach strong coupling without a significant emission quenching. Then, I will simulate the behavior of Ag and Au nanocube dimers while tuning the nanocubes size and their interparticle distance. In this way I will optimize the design of plasmonic resonators in order to achieve strong coupling criteria while maintaining a large emission quantum yield at ambient conditions.
The calculations results clearly show that an excellent compromise between these two parameters can be found both for silver and gold nanocavities and the differences between the two systems will be analyzed in detail.

2

GOLD NANOCUBES

In this chapter I will provide an optical characterization of single gold nanocubes. Then, the experimental data will be compared with the results of a fully electrodynamic simulation of the system, in order to verify the validity of our estimations.
Gold nanocubes for the preliminary analysis had a nominal side length of 55nm and were provided by Sylvie Marguet (CEA Saclay), habitual collaborator of the team. These nanoparticles are passivated by positively charged amphiphilic molecules (Cetrimonium bromide or CTAB) that form a bilayer on the nanoparticle surface. A second thiolated dodecamer alkyl ligand (C12)is also present to stabilize the sharp tips of the nanocubes and avoid their slow evolution towards nanospheres.

2.1 SEM IMAGING

Firstly, SEM characterization was performed to evaluate the shape and size distribution: $1\mu l$ of stock-solution was deposited onto a silicon substrate and analyzed with the field-electron-gun Scanning Electron Microscope of ESPCI Paris; the voltage applied to the field electron gun was equal to 10kV with a resulting current of 50pA. As it is possible to appreciate below, the nanocubes appear immediately homogeneous in size and rather sharp; the most regular particles tend to self-assemble in groupings, surrounded by the less cubic ones. Several images were treated through the software ImageJ, finding an estimated side length of 52±0.4 nm and curvature radius of 7.5±0.5 nm, with a percentage of perfectly cubic NPs higher than 70%.

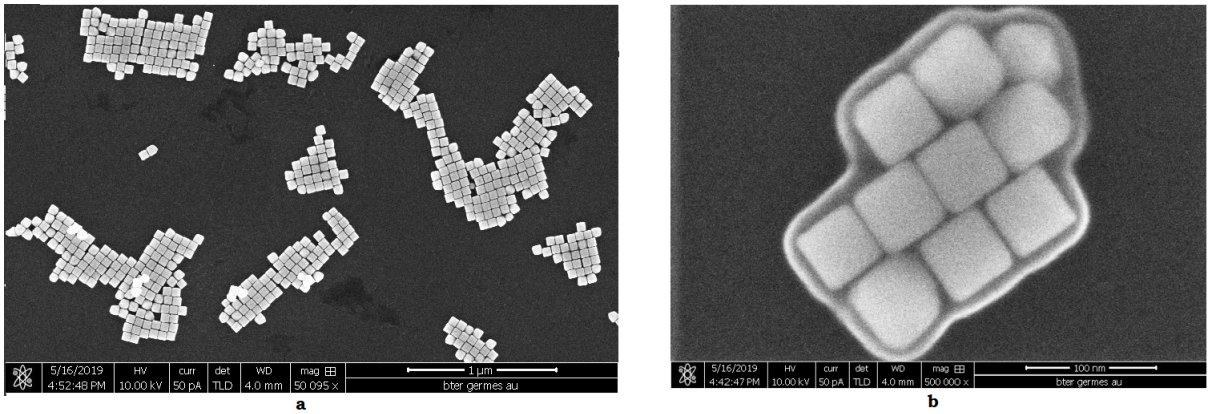

Figure 2.1: Sem images with different magnification scales. The halo surrounding the particles in (b) is due to the passivating bilayer (CTAB) on their surface that charges under the electron beam.

2.2 OPTICAL CHARACTERIZATION

2.2.1 *Extintion spectrum analysis*

The first optical characterization of nanocubes was performed through the HOSHIBA *Duetta* Fluorescence and absorbance spectrometer shown in figure 2.2a: 20 μl of mother solution were excited by a white light source and a CCD-photodetector collected the transmitted light straight through the sample; than a software processed the data, providing the extinction spectrum in

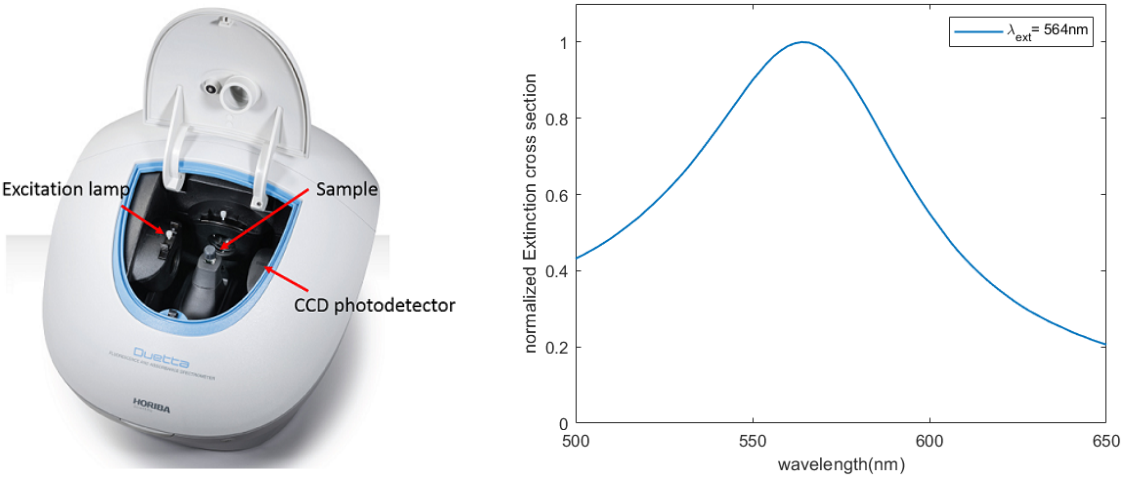

(a) (b)

Figure 2.2: (a)Duetta set-up; (b) Extinction spectrum

fig.2.2b. The resonance wavelength, equal to 562nm, corresponds to the average dipolar mode of the gold nanocubes in solution.

2.2.2 *Dark field scattering spectroscopy*

100 μl of 55nm-Au NCs mother solution were spin-coated on a freshly-cleaned glass coverslip in two steps: the first 5 seconds at 500rps (rounds par second) and then for 30s at 3000rps. Spin-coating was employed to avoid the formation of aggregates as observed in the SEM images for which the samples were let to dry in air.
The set-up for dark-field microscopy and spectroscopy is given by a classical inverted microscope (IX71, Olympus) with incoherent and non-polarized white light excitation.The excitation light is focused on the sample plane by means of an oil-condenser lens with Numerical aperture NA$\in [1.2 - 1.4]$ while the light scattered by nanoparticles is acquired through an oil lens with smaller NA (0.6), to avoid the collection of unwanted incident light. Then, the scattered light can be analyzed by a spectrometer (Roper, Princeton Instruments) or by a CCD photodetector, which allows a direct observation of the sample as shown in fig. 2.3a. Each orange point is an Airy spot corresponding to single nanocube observed with the point spread function of the microscope due to the diffraction limit. Less than 10% of points show a spectral red-shift, together with a larger intensity. They are likely to occur in correspondence of small aggregates of nanocubes. The light scattered by each NC can be directed also toward a spectrometer through a multimode fiber, with diameter equal to 50μm, acting as a pinhole for confocal spectroscopy. The latter one is fixed: it follows that the sample has to be fixed onto a piezoelectric plane that can be moved from the computer in order to align each point with the fiber aperture. The light entering in the spectrometer is dispersed according to its frequency and the raw scattering spectrum (S_{raw}) is obtained by the software WinSpec32 integrating the collected light. However, the background noise and the excitation spectrum (S_{back})have to be collected in a region without NCs and subtracted to the raw ones. Thus, the data have to be analyzed with Matlab: the final normalized spectra are evaluated as $S = \frac{S_{raw} - S_{back}}{S^*_{back}}$, where the denominator is smoothed in order to correct the spectrum from the spectral dependence of the light source and of the transmission of the microscope without decreasing the signal to noise ratio.
The 55nm Au-NCs spectra were measured with an integration time of 4s. During the measurements, spin coated nanoparticles were covered by an oil layer which provides an homogeneous

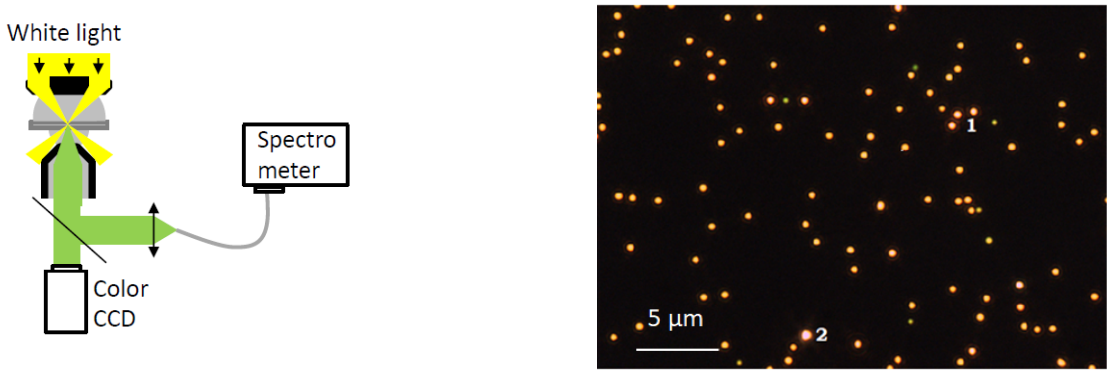

(a) (b)

Figure 2.3: (a) schematic representation of dark-field microscopy set-up; (b) dark field image of 55nm Au NPs spin coated on a glass coverslip, red points around 1 and 2 could show NCs aggregates

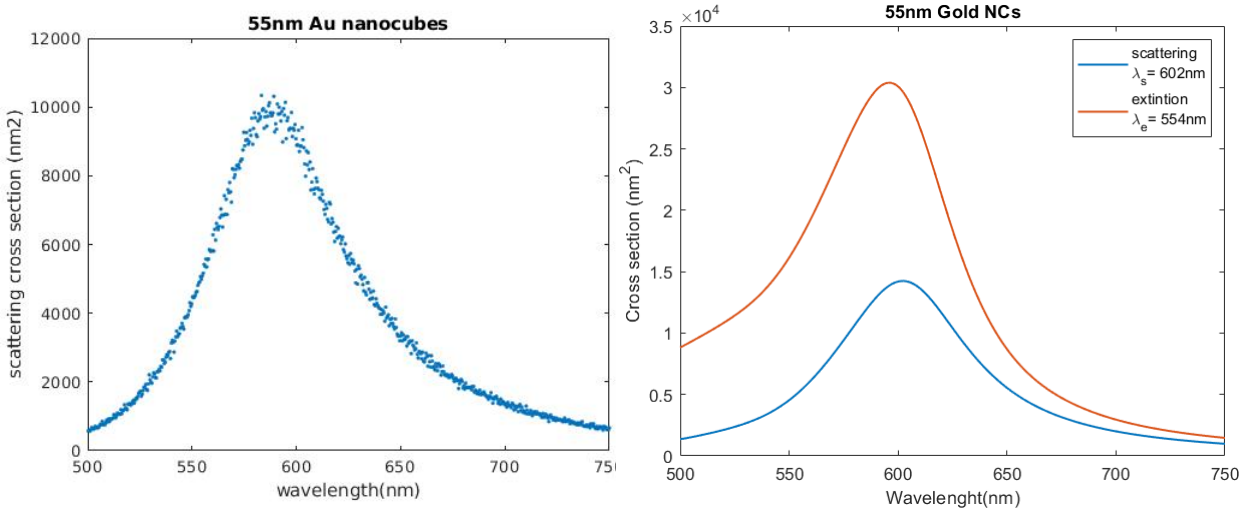

(a) (b)

Figure 2.4: (a) Example of a measured scattered spectrum; (b) simulated extinction and scattering cross sections of gold NCs with geometrical parameters s=52nm and $r_c = 97.5nm$

and isotropic dielectric function for the medium surrounding the sample.
Figure 2.4a shows the typical measured scattering spectrum of a 55nm Au-NC. It features a single bright mode, with resonance wavelength equal to 586nm. It falls in the orange portion of visible range, as expected according to fig. 2.3b. It is ∼20nm red-shifted w.r.t the extinction spectrum in fig. 2.2b, basically due to the convolution of two effects. First of all in the extinction measurement NCs were in an aqueous solution ($\epsilon_d \sim 1.33$) while in the latter one they were surrounded by oil($\epsilon_d = 1.5$). Contrarily, the second reason is intrinsically connected with gold nature: absorption resonance in this metal is always slightly blue-shifted w.r.t scattering for the presence of interband transition, as it will be discussed later.

Now let's compare them with the theoretical expectations obtained by means of the MNPBEM matlab toolbox[23], specifically designed for the fully-electrodynamic simulation of metal nanoparticles (MN) and based on the Boundary element method (BEM). [1] A single nanocube was modeled with the geometrical parameter found through the SEM images (s=52nm, r_c=7.5nm) and the environment dielectric constant was set to 1.5 to take into account the presence of the oil layer.

1 It is suitable to treat only objects with an homogeneous dielectric function that are separated by an abrupt interface. The toolbox solves Maxwell's equations only at the bodies surfaces, i.e. the boundary alone have to be discretized and not the entire volume.

Then, the propagation and polarization of the incident plane-wave were set respectively parallel to x and z. However, the modeled cube was perfectly symmetric and thus isotropic, i.e. the optical response for this ideal system would be equal for all the possible combinations of propagation and polarization directions. The BEM solver computes the charge density on the surface of the nanoparticle and, through it, the power radiated by the gold NC, treated as a polarized dipole. This corresponds to the scattering cross section, while the extinction spectrum is evaluated from the induced dipole total dissipated power. The difference between extinction and scattering cross sections will give the absorption one, associated to heat-dissipation in the metal. The result of these calculations as a function of the incident wavelength is shown in fig. 2.4b. The scattering spectrum is in perfect agreement with the measured one, both in terms of intensity and bandwidth. The extinction cross section is obviously similar to fig.2.2b, even if its linewidth is less broadened than in the measured case: it is quite reasonable, since the simulation is referred to a single NC, while the Duetta set-up only allows for ensemble measurements in solution. For this reason the same problem is not present in the scattering case, as it will be demonstrated later through the Q-factor.As expected, extinction spectrum is slightly blue-shifted and much higher than the scattering one, especially around the resonance wavelength and below it, confirming the lossy nature of gold electronic oscillations. The remarkable asymmetric behavior of the extinction cross section is due to the interband electron transitions that in gold occur between 5d and 6s electronic levels and dominate the absorption coefficient ($2\epsilon_m^2$) for $\lambda < 550nm$. It follows that gold dielectric function cannot be described with the simple Drude model, suitable only for the free-electron metals. However, almost all the teams working with gold plasmonic structures exploit the $Jhonson\&Christy's$ experimental data set for it [19], finding perfect agreement with their observations. For this reason, simulations were carried out with a fit of these raw data (see fig. 3.2 in the following chapter). To have a more quantitative comparison between measurements and expectations, 60 experimental scattering spectra were fitted with a Lorentzian shape, finding an average resonance wavelength and an average Q-factor respectively equal to 589nm and 7.76. Fig. 2.5 reveal a good correspondence between them and the measured results: the Q factor perfectly falls in the spectra distribution, confirming the goodness of the damping factor given by $J\&C's$ data set. The predicted λ_{res} is $\sim$10nm higher than the mean one, but it is likely due to a mismatch between the ϵ_d set in the simulations and the experimental one.

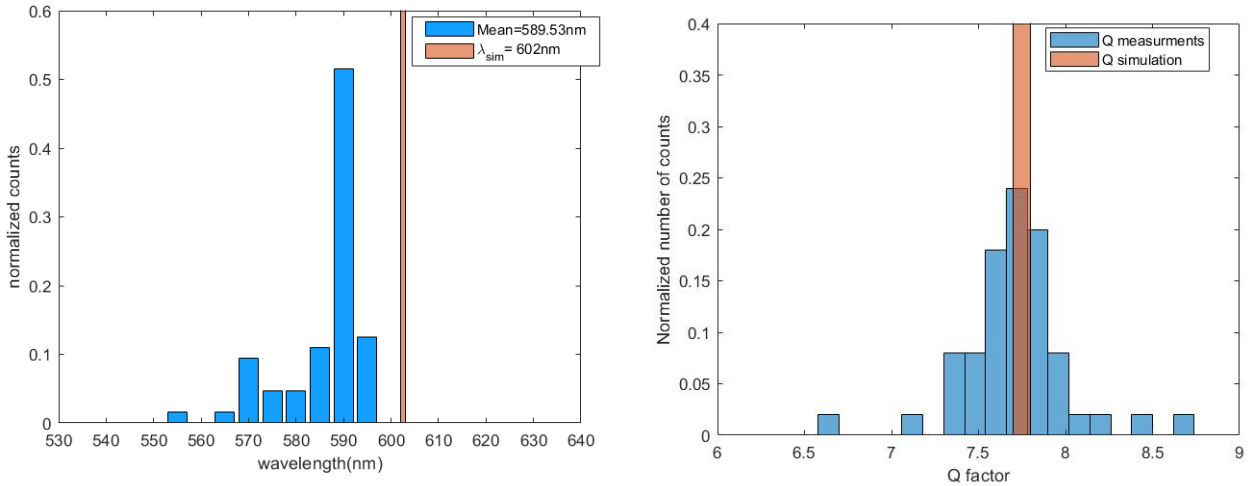

(a) (b)

Figure 2.5: Simulated values and experimental distributions of the (a) Resonance wavelengths and the (b) dipolar mode Q factors.

3

SILVER NANOCUBES

The high absorption cross section of gold nanocubes would cause an unavoidable quenching of the molecular emission. Given the less dissipative nature of Silver, the properties of Ag nanocubes were investigated, in order to verify their suitability to overcome this issue.

The same optical characterizations addressed in the previous chapter were performed on 75nm Ag NCs, already present in the lab and purchased from NanoComposix in solution in ehtanol with a concentration of 100mg/mL. They were passivated with PVP, a large polymer not easily displaced from the metal surface which offers good steric stability; it should help against the chemical etching of cubes edges caused by the high sensitivity of Ag toward oxidative processes. The investigation of SEM images provided by the manufacturers revealed an average curvature radius and a side length of about 9nm and 78nm respectively. Extinction and scattering spectra were assessed following the procedures depicted for gold,with few precautions: to prevent ultra-fast oxidation of spin-coated Ag-NCs, they were coated with oil immediately after their deposition on glass and not only during the scattering measurements; furthermore, due to the bigger size and thus the higher expected scattering cross section, the exposure time during the dark field microscopy was lowered to 2s.
Below, it is possible to see the Extinction spectrum of 75nm Ag NCs in aqueous solution and an example of single nanocube Dark field scattering spectrum. The resonance frequency of the first one is equal to 502nm,corresponding to the average dipolar modes of the particles in solution, and, also in this case, is blue-shifted with respect to the scattering one, due to the different background dielectric constant.

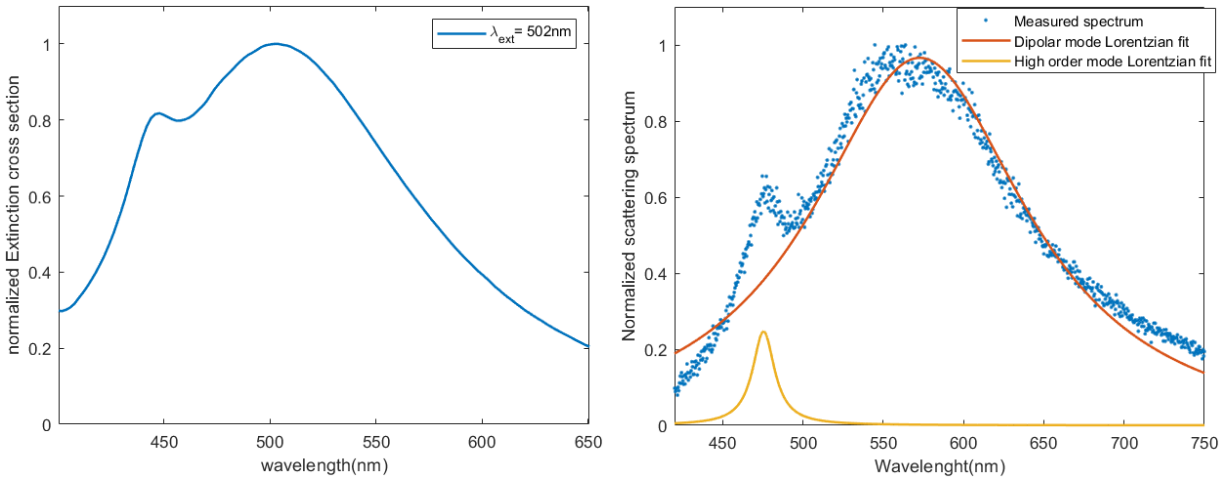

(a) (b)

Figure 3.1: (a) Extinction spectrum of 75nm Ag NCs in aqueous solution and (b) Example of single nanocube measured scattering spectrum. Dipolar and higher order mode were fitted with a Lorentzian shape.

However, the most evident feature of both fig. 3.1a and 3.1b is the presence of a secondary peak. Given the large NCs dimension, it is a high order mode appearing as a consequence of the retardation effects. It is well pronounced in both the extinction and scattering spectra, i.e. it is associated to both a large extinction and a large scattering cross section. On the contrary, in

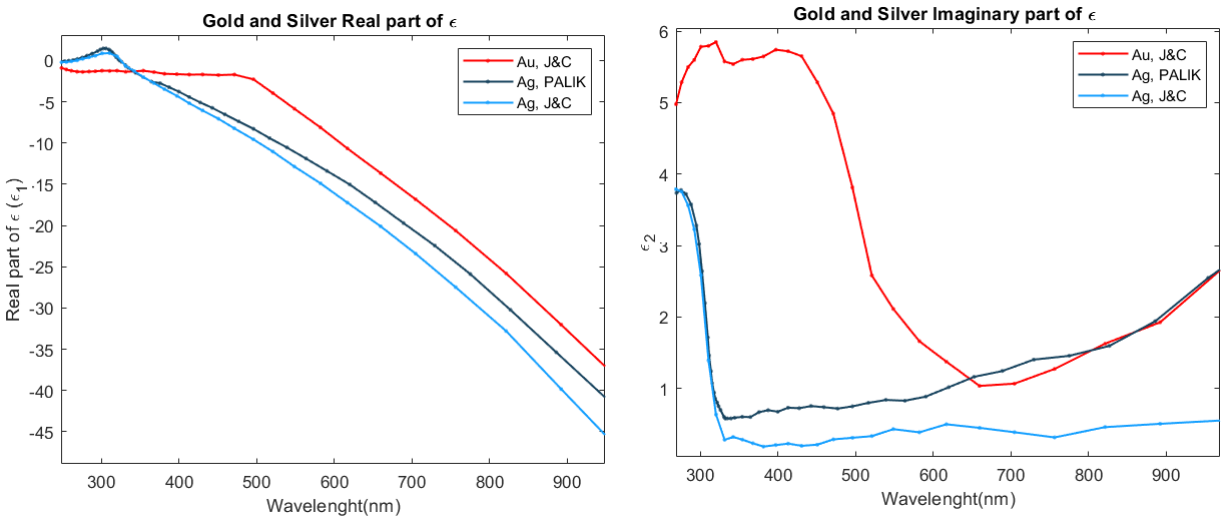

(a) (b)

Figure 3.2: Comparison between Palik and J&C (a) real and (b) imaginary part of the dielectric functions.

gold high order modes are more visible in extinction, since they barely scatter due to the high absorption coefficient of this metal. Thus, the presence of a still significantly bright high order mode in Silver spectra becomes the signature of its low heat dissipation.
Actually, in the plasmonic region of interest (the visible range) silver could be treated as a free-electron metal, since the interband transitions,occurring between levels 4d and 5s, play a significant role only at energy higher than 4eV. Nevertheless, in literature there is not a unique and unambiguous dielectric constant data set as in the case of gold. The most used among the community are Palik's and $J\&C's$ experimental data [19],[20] which are compared between them and with gold $J\&C's$ in figure 3.2.

As expected, both the Ag raw data set show the onset of interband transition for $\lambda < 300nm$, but for higher wavelengths the imaginary part of ϵ_{Palik} is much higher than $J\&C$'s one in the visible range and becomes even comparable with gold in the red and infrared ranges. This huge variability is due to the fast oxidation of silver in air, which makes the results to be strongly dependent on the environmental parameters.
Thus, I simulated the optical response of a nanocube (s=78nm, $r_c = 9nm$) embedded in oil and excited by z-polarized planewave, for both data-set. Then, to chose between them, I compared the calculated spectra with the experimental results. Figure ref. 3.3 shows the simulated extinction and scattering cross sections for 78 nm Ag NCs using Palik and $J\&C$ data sets. As a matter of fact, both the images show an higher ratio between scattering and extinction cross sections with respect to gold. It is reasonable, considering the bigger NC size and the low absorption of Silver w.r.t. gold in the considered optical range. However, in the blue part of the spectrum Palik's silver is, as expected, much lossier than J&C, causing the secondary peak to be significantly broader than the measured one and almost dark.
Moving to more quantitative analysis, the histogram in figure 3.4 shows a comparison between the simulated and experimental distributions of dipolar modes resonance wavelengths. Clearly, the average value is in between JC and Palik results. To explain why this phenomena occurs, let us consider for simplicity the case of a small silver sphere. As stated before, the resonance condition for such a NP is met for $\epsilon_1 = -2\epsilon_d$. Figure 3.2a clearly shows that ϵ_1 in the J&C's data set is lower (higher in absolute value) than for Palik's set of values.This means that the resonance condition for J&C will be met for a lower wavelength than for Palik, in agreement with the simulation.

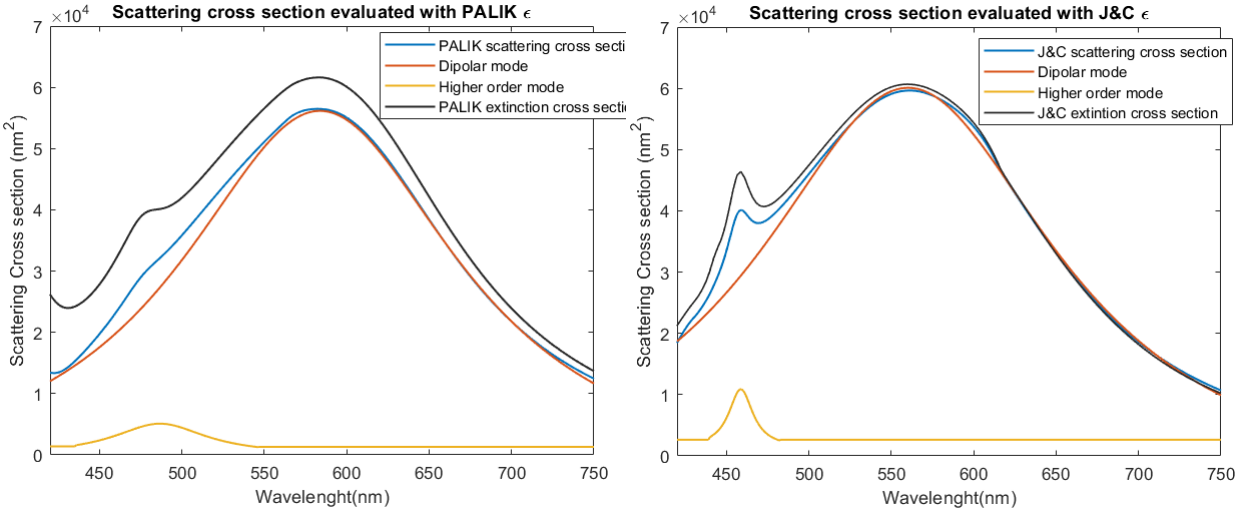

(a) (b)

Figure 3.3: Simulated extinction and scattering cross sections for 78 nm Ag NCs using (a)Palik and (b)$J\&C$ dielectric functions.

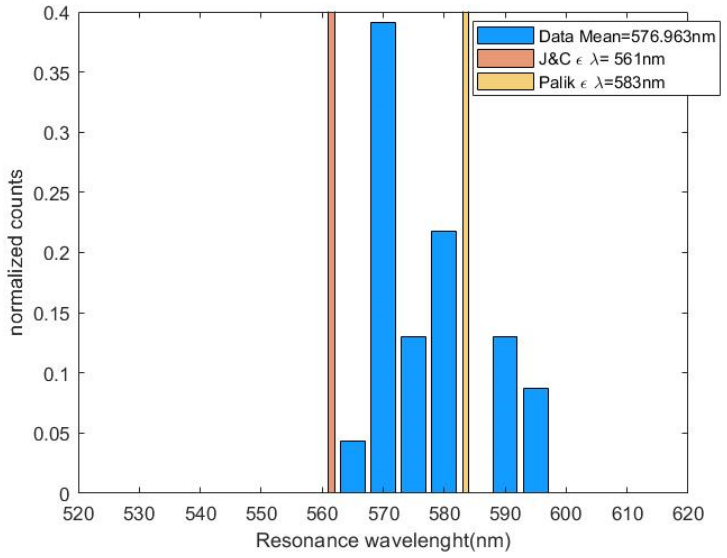

Figure 3.4: Simulated values and experimental distributions of the dipolar mode resonance wavelengths.

In figures 3.5a and 3.5b instead, it is possible to see the quality factor distributions of respectively the measured dipolar and higher order mode, together with their calculated values.
The two histograms demonstrate that the quality factor evaluated with Palik's data set is significantly lower than the experimental distribution for both the modes, proving its severe overestimation of the absorption coefficient. On the other hand, J&C's values provides a much better approximation of this parameter in the secondary peak case, but it still undervalues the dipolar quality factor. This could be due to a convolution of two effects. Again, it could slightly overestimate of the imaginary part of ϵ, but at the same time it certainty provides a higher scattering cross section , i.e a bigger damping, due to the larger absolute value of ϵ_1, which pushes up the refractive index difference between NP and environment.
More reasonable results have been found reducing the dielectric constant of the environment and with values of ϵ_1 in between ϵ_1^{PA} and ϵ_1^{JC} and for ϵ_2 slightly lower than ϵ_2^{JC}. The resonance wavelength in these conditions very well fits the experimental distributions, while the quality fac-

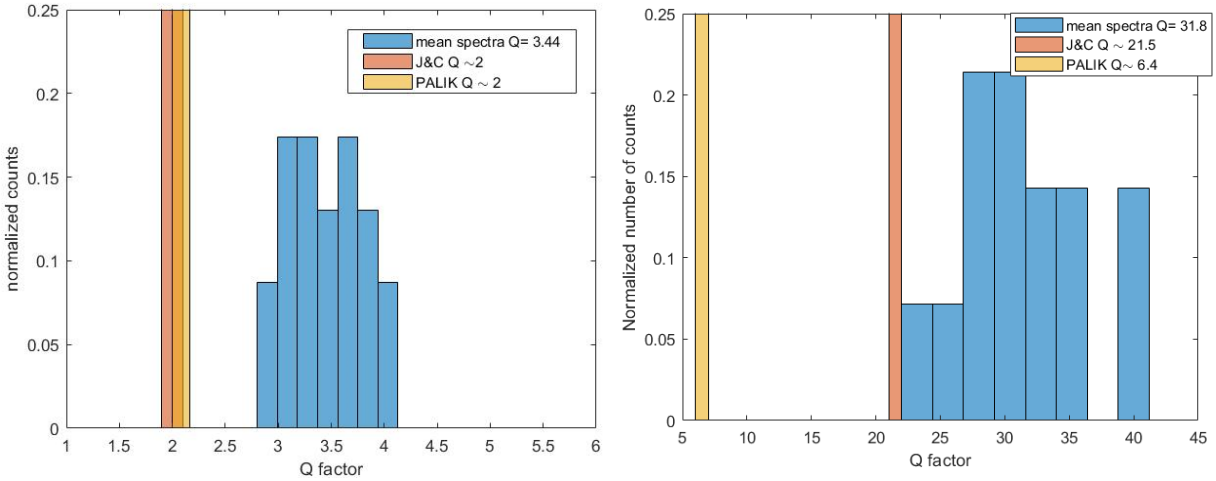

(a) (b)

Figure 3.5: Simulated values and experimental distributions of the (a) dipolar and (b) high order modes Q factors.

tor of the dipolar mode, still lower than the average measured value, is in better agreement with it.

However, being not tabulated values, we decided to not use them for the electrodynamic simulations of nanocubes dimers reported in the following chapter.
Then, since Palik's clearly overestimates non-radiative damping processes, the chosen set of values was again a fit of the J&C's one for both the real and imaginary part of ϵ.

4

NANOCUBES DIMERS

Despite the promising results of the preliminary optical tests, the high scattering cross section of 78nm Ag-NCs causes a too low quality factor of the dipolar mode. Then, its linewidth is in the order of 700meV, much bigger than the commercial dye molecules typical value($\sim 120meV$), actually preventing their use to reach strong coupling.
The aim of this chapter is to find an optimized configuration for the nanocubes dimers, which can provide at the same time a good enhancement of radiative LDOS and an acceptable damping rate. This is due not only to the employed metal: the interparticles distance strongly affects all the parameters entering in the coupling strength(see eq. 5), total Purcell factor, mode volume and cavity quality factor, but also the ratio between radiative and total density of optical state at the dipole position.
Unfortunately the latter one,which could be defined as a *Density of optical states yield* at the position of the molecule in the cavity[1], and Ω are not maximized together as it will be clear in the following pages. The MNPBEM tool, in fact, allows also to simulate the optical response of a point dipole placed in a structured environment. All the results obtained in this chapter are given by the simulation of a dipole placed exactly in between the tips of two nanocubes and oriented parallel to the dimer axis, in order to excite the longitudinal dipolar mode. The BEM solver computes the radiated and total dissipated power of a dipole placed in the modeled optical cavity. These two quantities, once normalized over the emitted power in a free environment, correspond to the enhancement of respectively radiative and total density of optical states at the emitter position, as stated in eq. 2.
Thus, it is possible to evaluate the evolution of the Purcell factor and the LDOS yield for several combinations of NCs size, composition and distance.

4.1 40nm nanocubes

The first simulated nanocavity was composed by two Ag-nanocube with side (s) and curvature radius (r_c) equal to 40nm and 5nm respectively, to be directly comparable with the already studied gold nanosphere dimers (diameter of 40 nm).
In figure 4.1a it is possible to appreciate the enhancement of the total density of optical states in the cavity as a function of the dipole emission wavelength, for d= 6nm,4nm,3nm. Shrinking the gap, dipolar modes of the single NPs start to couple more and more efficiently and the resonance frequency of the hybrid mode red-shifts (for a quantitative analysis see fig. 4.5a of section 4.3); the secondary peak occurring around $\lambda = 450nm$ is due to the hybridization of high order modes. It should be noticed that equation 3 is valid only for single mode cavity while, for sufficiently small gap, our plasmonic resonator shows at least two available modes. However, once found an optimized configuration, it will be possible to chose a dye molecule emitting exactly in the range of wavelength overlapped with the dominant mode, such that the coupling will occur only with it.

Figure 4.1b, instead, reports the evolution of Purcell factor at the resonant wavelength and the cavity quality factor as a function of the cubes distance. The system simulation for d=1nm

1 This name is due to the fact that it does not take into account the internal non radiative relaxation processes that, as explained in chapter 1.1, are not affected by the structured environment.

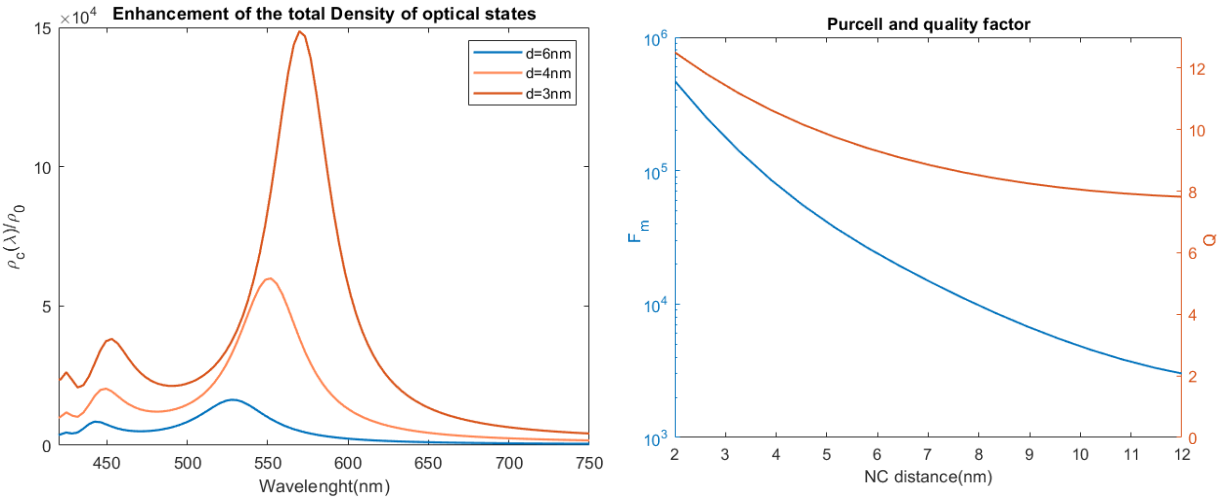

(a) (b)

Figure 4.1: (a) Enhancement of the LDOS for different interparticles distances; (b) Purcell and Quality factors as a function of d.

was not performed because at such a distance convergence of the iterative approach is not guaranteed;moreover, quantum effects such as electron tunneling between particles should be taken into account. The Purcell factor increases by more than 2 orders of magnitudes from d=12nm to d=2nm, strongly pushing up the coupling strength; in the meanwhile Q is only slightly increased, confirming the fundamental role of the mode volume reduction.
Please notice that the above discussed trends are valid independently on the material and side length of the NCs involved. To understand the effects of these parameters on the behavior of the coupled system, it is necessary to analyze how the enhancement of total and radiative DOS at the resonance frequency and the cavity quality factor evolve as a function of d, case by case.
This has been done in figure 4.2a for silver and gold 40nm NCs dimers: clearly, the radiative decay channels are predominant in Ag, anticipating the very high LDOS yield reported in the left side of the same picture. However, a silver system of these dimension still exhibits high scattering cross section, significantly affecting the quality factor: it makes both the total density of optical states and the coupling strength to be lower than in gold. Thus, this configuration would be a perfect optical antenna for the conversion of far field radiation into localized energy and vice-versa, but is not worthwhile for the strong-coupling regime.

The only way to decrease the scattering cross section is to reduce the particles dimension; unfortunately, as briefly mentioned at the beginning of chapter 3, silver nanocubes corners are extremely sensitive to oxidative etching processes and for this reason the synthesis of smaller Ag-NCs, as well as their surface chemistry modification remain challenging. Nevertheless, in 2013 Yi Wang and colleagues published a possible protocol for the fabrication of 32-28-23 and 18nm Ag-cubes [21]: they substituted the commonly used solvent in Ag-NPs synthesis with a longer chain one, with an higher viscosity and a lower reducing power w.r.t its precursor. Even if this approach is not yet robust and reliable as the one available for gold, the possibility to produce 30nm Ag NCs justified the choice to simulate their behavior.

4.2 30nm silver nanocubes

Passing from 40 to 30nm side length, r_c was lowered to 4nm. According to the Lightning rod effect, the increased curvature will further enhance the electric field in the gap, i.e. the radiative

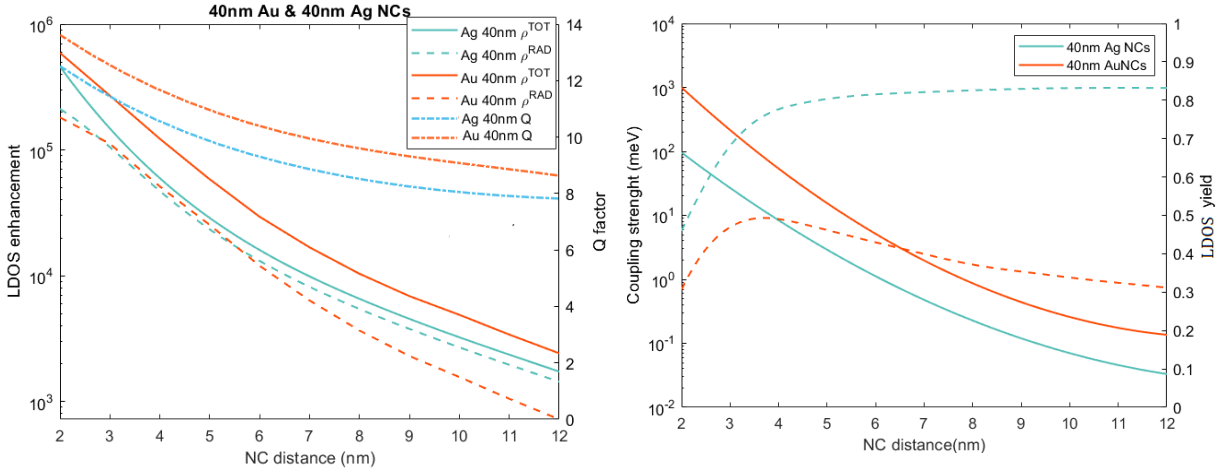

(a) (b)

Figure 4.2: (a) Radiative and total LDOS enhancement (the latter one is equivalent to the Purcell factor) and (b) coupling factor and LDOS yield of Ag and Au 40nm NCs dimer as a function of d.

LDOS. This, together with the magnified Q factor (see the picture on the left) and the lowered mode volume, should highly push up the Purcell factor and therefore the coupling strength. Figure 4.3b distinctly confirms this expectation: Ω_{30nm}, always at least one order of magnitude larger than Ω_{40nm}, exceeds $10^5 meV$ when d=3nm; then, contrarily to what happens for 40nm Ag or Au NCs, it starts decreasing. The quality factor, in fact, being significantly higher than before, makes the mode linewidth for $d < 3nm$ lower than the molecular one, causing the denominator in eq.5 to increase. Remarkably, the strong-coupling regime should be reached already for d∼10nm; however, the visibility criterion would require lower distances.

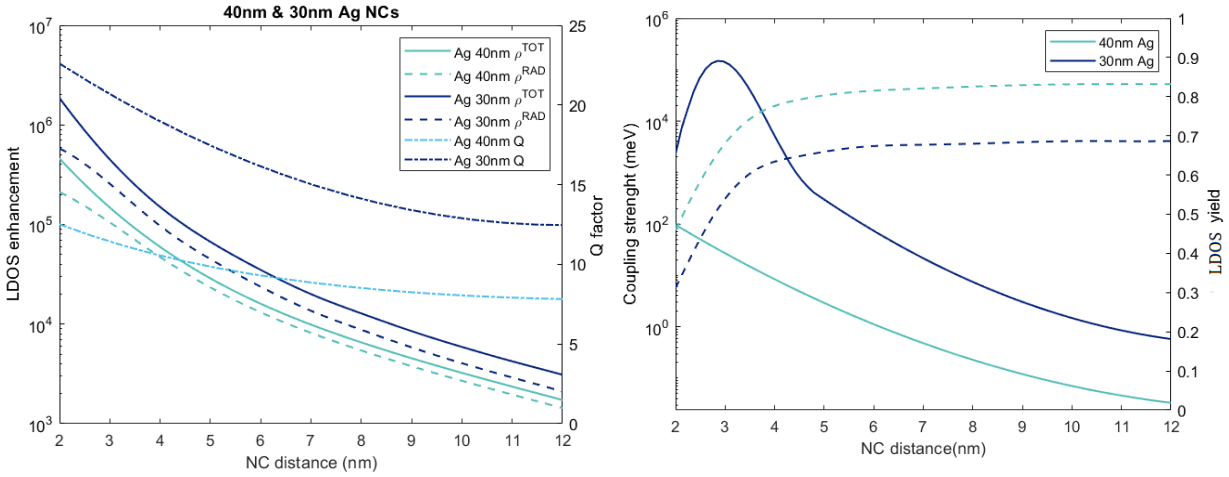

(a) (b)

Figure 4.3: (a) Radiative and total LDOS enhancement (the latter one is equivalent to the Purcell factor) and (b) coupling factor and LDOS yield of Ag 30 and 40nm NCs dimer as a function of d.

Unfortunately, also in this case an higher coupling strength corresponds to a lower LDOS yield. Indeed, to obtain such a huge Purcell factor, the number of non-radiative decay paths increased as well and, as shown in fig. 4.3a, in higher percentage w.r.t. the radiative channels; this is easily understandable invoking again the reciprocity principle- since smaller nanoparticles, all the other factor being equal, are always associated with larger absorption cross section ($\sigma_{ext} - \sigma_{sca}$). Nevertheless, at least for d≥3nm it is still significantly higher than the 40nm Au-NCs one,

confirming the promising nature of this configuration, especially for d=3nm where the coupling strength is incredibly high while $\rho_p/\rho_0 > 0.5$.

4.3 30nm gold nanocubes

Due to the more robust fabrication process of gold nanocubes in the range between 17and 78nm [22], their higher achievable sharpness and steric stability making it preferable to silver, also the change in optical environment between two 30nm Au cubes was simulated.
Figure 4.4a reveals that also in this case the volume reduction, lowering the scattering cross section, causes an improvement in the quality factor. However, given the intrinsically lossier nature of gold w.r.t silver, this effect is much less pronounced than before and the Purcell factor of the two structures are almost equivalent everywhere except for very low interparticles distances. For this reason, even if the coupling strength is always higher than for 40nm gold NCs, it does not exceed $2 \times 10^4 meV$, as visible in fig. 4.4b. Nevertheless, the main drawback of this configuration is an almost total quenching of the emitter emission: the LDOS yield does not exceed 0.1, showing a reduction of 80% with respect to the 40nm case, unacceptable if compared to 20% reduction occurring in silver for the same length scaling.

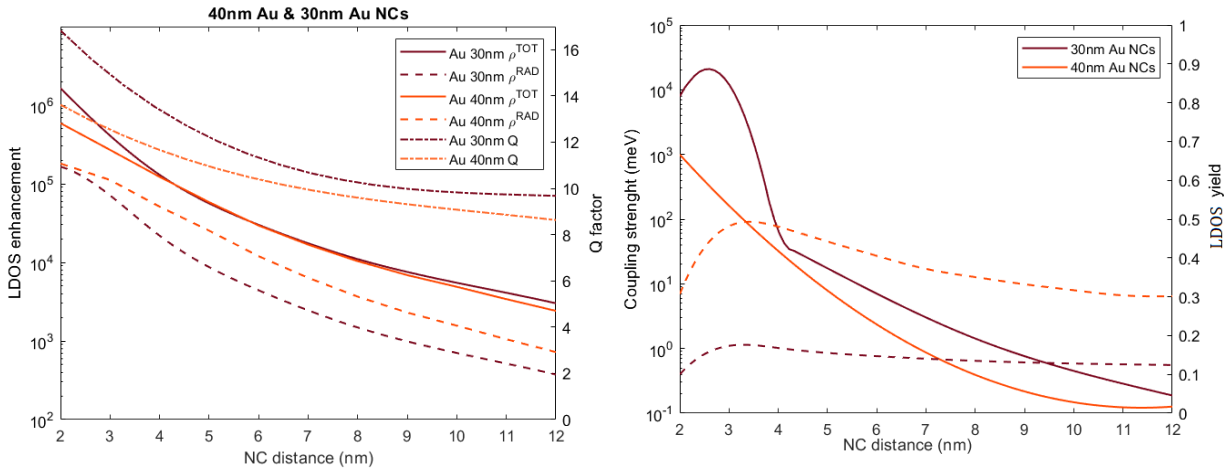

(a) (b)

Figure 4.4: (a) Radiative and total LDOS enhancement (the latter one is equivalent to the Purcell factor) and (b) coupling factor and LDOS yield of Au 30 and 40nm NCs dimer as a function of d.

It is clear that the explanation for this dramatic drop-off and the reason why it does not occur in silver have to be found in the intrinsic material properties,i.e. in the imaginary part of their dielectric function.
In figure 4.5a the evolution of the expected resonance wavelengths as a function of the interparticles distance is reported for the four analyzed configurations. As briefly explained before, shrinking the gap leads to a red-shift of λ_{res}, due to the increased coupling strength which lowers the hybrid mode energy. In both cases, passing from 30nm to 40nm of side size the resonance wavelength of the coupled systems increases for each d; however, 4 marker points were placed in correspondence of d=3nm, since it seems to be the most promising gap length. Starting from 4nm, in fact, all the structures experience a reduction of the LDOS yield and d=3nm guarantees high coupling strength with a still acceptable radiative LDOS except, naturally, for 30nm Au NCs.

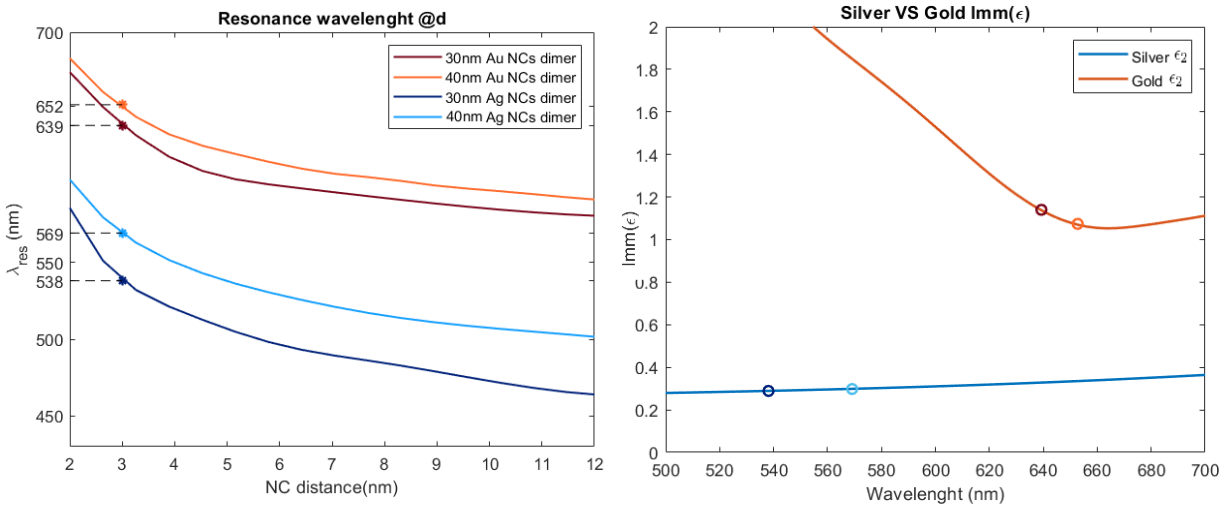

(a) (b)

Figure 4.5: (a) Resonance wavelength evolution as function of NCs distance (b) Silver and Gold imaginary part of ϵ. The highlighted circles correspond to ϵ_2 at d=3nm for each configuration. The marker colors are coherent with the left picture.

Figure 4.5b shows the behavior of the imaginary part of ϵ for both the metals in the range of interest and finally explains why they behave so differently: while the ϵ_2 of Ag is almost constant between 500nm and 700nm, the ϵ_2 of Au rapidly decreases before 660nm; this implies that 30nm Au NCs inevitably have a much higher absorption coefficient tha 40nm Au one, while in silver it is only slightly modified and,moreover, reduced: for d=3nm $\epsilon_2^{Au30} - \epsilon_2^{Au40} \sim 0.1$ while $|\epsilon_2^{Ag30} - \epsilon_2^{Ag40}| < 0.01$. For this reason the radiative decay paths in 30nm Au NCs cavity are even lower than the already limited channels of 40nm gold structure, making this system completely unsuitable for our purposes.

4.4 OPTIMAL STRUCTURES

The straightforward conclusion of the previous investigations is that for gold and silver the optimal structures are 40nm and 30nm NCs respectively. As observed below, a direct comparison between their coupling strength and LDOS yield unambiguously shows that the latter one would be highly preferable for both of them.

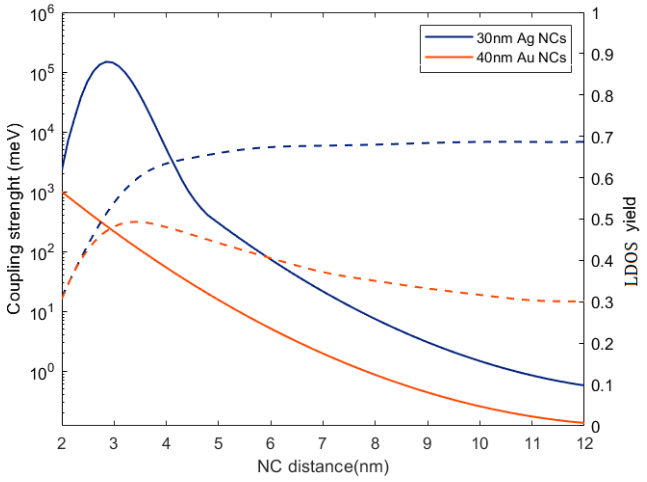

Figure 4.6: Coupling strength and LDOS yield for 40nm Au and 30nm Ag NCs dimer

However, as already stated several times, such small silver NPs present stability and fabrication issues which make their use in origami based assembly more difficult. It is interesting to note that the assembly of dimers of Ag nanospheres was recently achieved by Acuna and coworkers [27]. The assembly of 30nm Ag NCs is therefore an exciting perspective if the assembly of Au NCs is achieved.

As a consequence, part of my internship was devoted to learn the chemical procedure for the DNA-mediated self-assembly of gold NPs, starting from 40nm-gold spheres. In the following chapter I will address this technique and the difficulties that appeared when switching from spheres to cubes.

5

SYNTHESIS OF GOLD DIMERS AND FUTURE PERSPECTIVES

5.1 40nm spheres dimers

Commercial Au NSs are covered by negative citrate ions. However, they avoid nanoparticles aggregation only for relatively low concentration ($9 \times 10^{10} mL^{-1}$) while the protocol to efficiently produce dimers needs colloidal solutions 100times more concentrated. Thus, the first step of the procedure is to introduce BSPP (bis(p-sulfonatophenyl)phenylphosphine), that easily displaces citrate since the interaction between phosphine and gold is thermodynamically favored; being negatively charged, this new ligand stabilizes the colloidal solution by means of strong electrostatic repulsion.
The following step is the attachment of DNA strands on gold surface; since Au-S bond is stronger than Au-P, this can be done introducing in solution a proper amount of DNA-single strands functionalised at one termination with 3 thiol groups. This procedure is done for two set of NSs: the first one is functionalized with a bare DNA-strand, while the other with a complementary DNA sequence, containing 5 ATTO647N molecules in the desired position. In the first case the number of DNA strands par NP has to be high enough to maximize the probability to obtain a dimer; contrarily, the ratio between 5ATTO647N-strands and NSs has to be as low as possible, ideally approaching 1. This is necessary to avoid the presence on the dimer surface of supplementary dye molecules, that could cause an increase of the coupling strength between the in-gap emitters and dipolar mode of the cavity.
It is worthy to notice that both NSs and DNA strands are negatively charged: to force their interaction it is necessary to act on the solution salinity, introducing cations Na^+ that will screen their repulsion. Experimentally it has been found that for a $10\mu L$ of solution with $2\mu L$ of 40nmAU NSs (20nM) the right amount of NaCl is 25mM.
After one night of incubation, the metal surface is further passivated by an excess of functionalized thiolated/methyl terminated ethylen glycol oligomers (m-PEG for 5ATTO647N-DNA samples and bio-PEG for the bare DNA case), which provide a steric stabilization of the solution.
Before proceeding with the complementary DNA-strands hybridization,i.e. with particles dimers formation, monomers have to be purified from the excess of ligands in solution and NPs with a single DNA strand have to be separated from the other. This can be done by means of electrophoresis, a technique that exploits the difference of diffusion velocity between different biomolecules traveling in an aqueous gel under an applied electric field(∼5V/cm for 40min). NPs with no or a limited amount of attached DNA will feature a lower hydrodynamic volume than particles entirely covered with DNA and will diffuse faster in the gel.
The latter one is prepared with a solution of Agarose in TBE, tris-borate EDTA buffer solvent, whose concentration is fundamental for the particle mobility inside it (for 40nm single NS, it has to be around 1% in weight).
Figure 5.1(a) reports an example of Gel were it is clearly visible the effect of DNA concentration. Columns 1-2-3(respectively 4-5-6) are functionalized with an increasing concentration of 5ATTO647N- DNA strands (bare DNA strands). The exact number of DNA strands par each NP cannot be exactly known, since it is described by a Poissonian distribution centered in $\overline{n} = 0, 1, 2....$ Increasing this number,the NPs get larger,entering less easily in the gel. Thus, the red and thick slices in figure correspond to the lowest possible $\overline{n}$; they are separated from the gel by applying $\sim 11.5 V/cm$ for a short time and rinsed. At this point the complementary set of

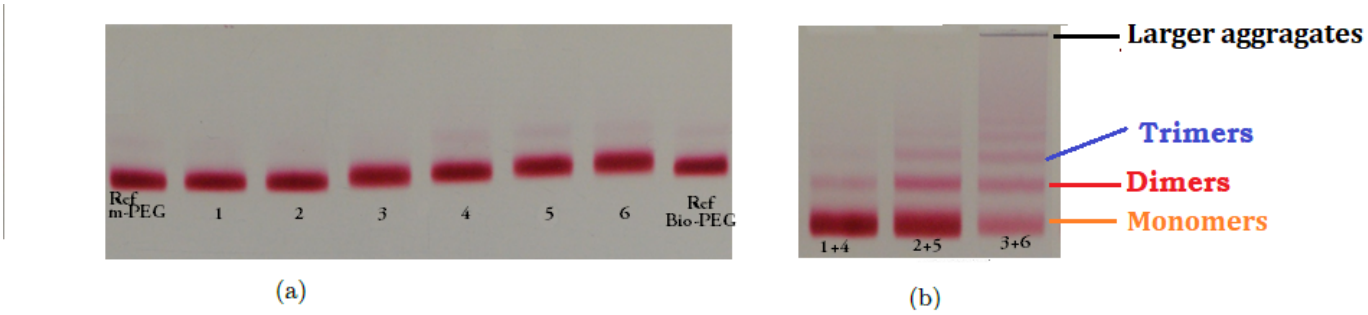

Figure 5.1: (a) single particles gel. The two references are NPs without DNA, functionalized with m-PEG and bio-PEG respectively. Clearly, bio-PEG is heavier than m-PEG. 1-2-3 NPs functionalized with a crescent density of 5ATTO647N DNA single strands. 4-5-6 NPs functionalized with a crescent density of bare DNA single strands.
(b) Hybridized particles gel. Increasing the amount of DNA par sphere, the number of multiple hybridization (trimers, quadrimers) and aggregation increases.

NPs are sufficiently pure and can be hybridized to obtain particles dimers.
Naturally, higher is the starting $\overline{n}$, higher will be the probability of bigger aggregates (trimers etc.). Thus, after another night of incubation, the new suspensions are once again purified by electrophoresis to isolate the dimers from the undesired configurations. Given the bigger volume of dimers w.r.t. single NPs, the concentration of the gel is lowered to 0.75%, to let the NPs enter inside it. Again, the effect of the initial DNA concentration is evident (see fig. 5.1(b)): the first column (samples 1+4) contains almost only monomers, demonstrating that for the starting samples $\overline{n}$ was close to 0. Contrarily, the last column (samples 3+6) shows a much lower amount of monomers, but a consistent number of trimers and larger aggregates which, in the biggest cases, are not able to enter the gel.
Dimers are isolated and separated again from the gel. At the end of the procedure, dimers in figure 1.5b are formed and ready for optical characterization.

5.2 CUBES DIMERS

Nanocubes dimers chemical assembly requires a different approach with respect to the above discussed protocol,due to the necessity to align the nanocubes from their vertexes. Differently from the nanosphere case, now the DNA hybridized strands with the dye molecules in between cannot link in a random point on the nanoparticle surface. For this reason it was necessary to commission a DNA-origami template [24] to Gaetan Bellot and his coworkers (CBS, Université de Montpellier), regular collaborators of the team. A scheme of the final structure is shown below: it provides two docking sites properly designed to host "tipped" nanoparticles, independently on the overall shape and, particularly interesting, size of them. This makes them perfectly suitable for our purposes, since it would let us to investigate the different cavity configurations (30nm-40nm Ag- Au NCs dimers) without purchasing several DNA-templates. Unfortunately, due to the necessity to put the emitter precisely in the middle of the gap, the group of G. Bellot was forced to split the DNA-template in two parts, one of them containing the dipole in the desired position(see fig.5.2); this made the fabrication to be more time-consuming and our collaborators were not able to provide yet the overall structure.
An additional difficulty in the assembly protocol is given by the different surface chemistry of gold NCs: during the fabrication process they are passivated with CTAB and C12, the latter strongly bounded to gold surface by means of a thiol group. For this reason DNA-thioleted

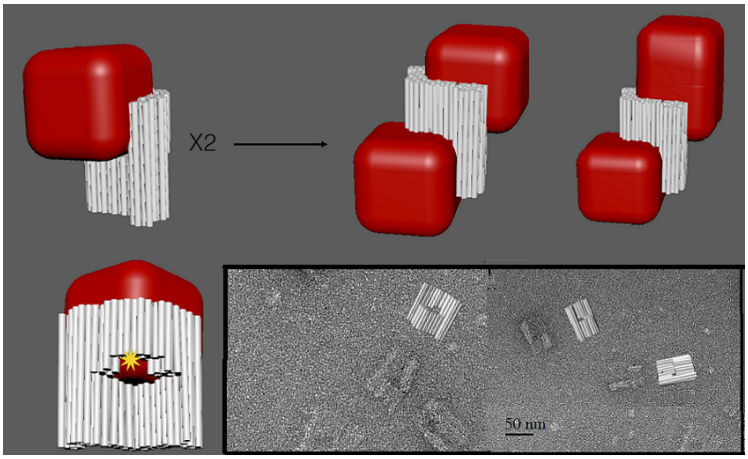

Figure 5.2: Assembly process for DNA-templated nanoparticles dimers with an emitter in between. The inset shows a negative stained-TEM image of the template

strands cannot easily displace C12 molecules, making the ligand-exchange process difficult; a strategy to overcome this issue is currently in development.

5.3 CONCLUSION AND FUTURE PERSPECTIVES

The following steps in the experimentation will be to assemble a single 55nm-Au cube with one half of the DNA-template, containing a single ATTO647N molecules at a distance from the tip equal to 5nm. The simulations carried out in this conditions show an enhancement of the field in this position approximately equal to 5 and an interaction strength in the weak-coupling regime. Then, once acquired the total DNA-template structure and found a reliable protocol for its assembly with gold NCs, the team will proceed with the optical characterization of the NCs dimer-emitter coupled system.

I am confident that gold 40nm Au-NCs dimer can provide an optical cavity with a quality factor at room temperature sufficiently high to reach strong coupling with a single dye molecule and still featuring an acceptable yield.
However, I strongly believe that Silver nanostructures could allow the optical platform for unprecedentedly high coupling strength and emission efficiency; improving Ag-nanoparticles bottom-up fabrication process and their colloidal stability would be of fundamental importance to obtain an highly non-linear optical system at room temperature.

REFERENCES

[1] T. Hugall,A. Singh, and N.F. van Hulst "Plasmonic cavity coupling".*ACS Photonics,5,43-53 (2018)*

[2] Grob et al "Near field strong coupling of single quantum dots". *Sci. Adv;* **4** *(2018)*

[3] D. Bouchet, R. Carmiati. "Quantum dipole emitters in structured environment: a scattering approach: tutorial" *Journal of the optical society of America A, Vol.36, No.2 (2019)*

[4] P Törmä and W L Barnes "Strong coupling between surface plasmon polaritons and emitters: a review" *Rep. Prog. Phys.* **78** *013901 (2015)*

[5] R. Carminati,A.Cazéb, D.Caoa, F.Peraguta, V.Krachmalnicoffa, R.Pierrata, Y.DeWildea "Electromagnetic density of states in complex plasmonic systems" *Surface ScienceReports,70,1–41(2015)*

[6] C. Sauvan, J. P. Hugonin, I. S. Maksymov and P. Lalanne. "Theory of the Spontaneous Optical Emission of Nanosize Photonic and Plasmon Resonators." *Physical Review Letters, American Physical Society,110 (2013)*

[7] J.J Greffet "Nanoantenna for light emission " *Science, Vol. 308, Issue 5728 (2005)*

[8] Hood, Chapman, Lynn, Kimble "Real time Cavity QED with single atoms." *Phys. Rev. Lett.,80(19),(2005)*

[9] G. Khitrova, H. M. Gibbs, M. Kira, S. W. Koch, A. Scherer. "Vacuum Rabi splitting in semiconductors" *Nature Physics, 10.1038/nphys227 (2006)*

[10] J. Bellessa, C. Bonnand, J. C. Plenet, and J. Mugnier "Strong Coupling between Surface Plasmons and Excitons in an Organic Semiconductor" *Phys. Rev. Lett. 93, 036404 ,(2004)*

[11] K. Santhosh, O. Bitton, L. Chuntov, G. Haran. "Vacuum Rabi splitting in a plasmonic cavity at the single quantum emitter level." *Nature Communications 7:118223 (2016)*

[12] R. Chikkaraddy, B. Nijs, F. Benz, S. Barrow, O. Scherman, E. Rosta, A. Demetriadou, P. Fox, O. Hess, J. Baumberg. "Single-molecule strong coupling at room temperature in plasmonic nanocavities" *Nature, Vol.5357 (2016)*

[13] H. Leng1, B. Szychowski2, M. Daniel2, M. Pelton "Strong coupling and induced transparency at room temperature with single quantum dots and gap plasmons" *Nature Communications 9:4012(2018)*

[14] Lukas Novotny, Randy X. Bian, and X. Sunney Xie "Theory of Nanometric Optical Tweezers" *Phys. Rev. Lett. 79, 645 (1997)*

[15] Mickaël P. Busson, Brice Rolly, Brian Stout, Nicolas Bonod , Sébastien Bidault "Accelerated single photon emission from dye molecule-driven nanoantennas assembled on DNA". *Nature Communications,3:962 (2012)*

[16] S. Bidault, A. Devilez, V. Maillard, L.Lermusiaux, J.M. Guigner, N. Bonod, J. Wenger "Picosecond Lifetimes with High Quantum Yields from single photon emitting colloidal nanostructures at room temperature" *ACS Nano 10, 4(2016)*

[17] Luis J. Mendoza Herrera, David Muñetón Arboleda, Daniel C. Schinca, and Lucía B. Scaffardi. "Determination of plasma frequency, damping constant, and size distribution from the complex dielectric function of noble metal nanoparticles" *Journal of Applied Physics* **116**, *(2014)*

[18] U. Kreibig and M. Vollmer "Optical properties of metal cluster", *Springer series in Material Science, 25,ch.2 (1957)*

[19] P. B. Johnson and R. W. Christy "Optical constants of the noble metals" *Phys. Rev. B 6, 4370 (1972)*

[20] E.D. Palik "Handbook of optical constants of solids". *Academic Press, (1997)*

[21] Y. Wang, Y. Zheng, C.Z. Huang, Y. Xia "Synthesis of Ag Nanocubes 18-32nm in Edge lenght: The effects of Polyol on Reduction Kinetics, Size Control and Reproducibility" *J Am Chem Soc;135(5) (2013)*

[22] J. Park, Y.Lee, J.M. Nam "Precisely shaped, Uniformely Formed Gold Nanocubes with Ultrahigh Reproducibility in Single-particle scattering and Surface enhanced Raman Scattering". *Nano Lett.18,10(2018)*

[23] U. Hohenester, A. Thrugler "MNPBEM- A Matlab toolbox for the simulation of plasmonic nanoparticles." *Comp. Phys. Commun.***183**, *(2012)*

[24] F. Hong, F. Zhang, Y. Liu, H. Yan "DNA origami: scaffolds for creating higher order structures" *Chem. Rev. 117,20(2017)*

[25] D. Baranov, M. Wersall, J. Cuadra, T. Antosiewicz, T. Shegai "Novel nanostructures and material for strong light-matter interactions" *Acs photonics 5,24-42 (2018)*

[26] G. Zengin, G.Johansson, P.Johansson, T. Antosiewicz, M. Kall, T. Shegai "Approaching the strong coupling limit in single plasmonic nanorods interacting with J-aggregates" *Scientific report 3,3074 (2013)*

[27] C. Vietz, I. Kaminska, M.S. Paz, P. Tinnefeld, G. Acuna. "Broadband fluorescence enhancement with self-assembled Silver nanoparticle optical antennas" *ACS nano,11,5,4969-4975 (2017)*